Lattice constraints on the thermal photon rate

J. Ghiglieri, O. Kaczmarek, M. Laine, and F. Meyer

Phys. Rev. D **94**, 016005 — Published 28 July 2016

DOI: 10.1103/PhysRevD.94.016005

BI-TP 2016/01

Lattice constraints on the thermal photon rate

J. Ghiglieri[a], O. Kaczmarek[b], M. Laine[a], F. Meyer[b]

[a]*AEC, ITP, University of Bern, Sidlerstrasse 5, 3012 Bern, Switzerland*

[b]*Faculty of Physics, University of Bielefeld, 33501 Bielefeld, Germany*

Abstract

We estimate the photon production rate from an SU(3) plasma at temperatures of about $1.1T_{\rm c}$ and $1.3T_{\rm c}$. Lattice results for the vector current correlator at spatial momenta $k \sim (2{-}6)T$ are extrapolated to the continuum limit and analyzed with the help of a polynomial interpolation for the corresponding spectral function, which vanishes at zero frequency and matches to high-precision perturbative results at large invariant masses. For small invariant masses the interpolation is compared with the NLO weak-coupling result, hydrodynamics, and a holographic model. At vanishing invariant mass we extract the photon rate which for $k \gtrsim 3T$ is found to be close to the NLO weak-coupling prediction. For $k \lesssim 2T$ uncertainties remain large but the photon rate is likely to fall below the NLO prediction, in accordance with the onset of a strongly interacting behaviour characteristic of the hydrodynamic regime.

1. Introduction

The intensity and spectral properties of the photons that are emitted from a thermal QCD plasma constitute excellent probes for the interactions that the plasma particles experience. Consequently, observing a thermal component in the photon yield of heavy ion collision experiments is among the main goals of the on-going program [1–3]. Simultaneously, on the theory side, the thermal photon rate has served as a classic testing ground for developing increasingly advanced computational tools [4–11].

In order to test thermal QCD in a model-independent way, we would like to compare first-principles computations with experimental heavy-ion data. Apart from difficulties related to large non-thermal backgrounds, this goal is faced with formidable challenges on the theory side. On one hand, QCD continues to be strongly coupled in the temperature range reached in practice, so that a weak-coupling expansion may not suffice for obtaining quantitatively accurate predictions (unless a very high order is reached, cf. e.g. ref. [12]). On the other hand, lattice QCD is not directly applicable either, because simulations are carried out in Euclidean spacetime, and analytic continuation to Minkowskian signature represents a numerically ill-posed problem (though the problem is again surmountable in principle [13]).

In the present paper, we suggest and test a pragmatic workaround to these challenges, which could lead to a relatively reliable practical estimate of the photon production rate in the temperature range accessible to the current generation of heavy ion collision experiments. The idea is to combine lattice and perturbative techniques, but only in regimes where they should be well under control. Concretely, this means that we make use of the weak-coupling expansion in the regime of large "photon masses", $M \gtrsim 1$ GeV, where the series shows reasonable convergence thanks to asymptotic freedom and the high loop order that has been reached. This "hard" component permits for us to reproduce the continuum-extrapolated lattice measurements at small imaginary-time separations. In contrast, at large imaginary-time separations the lattice data show clear deviations from the weak-coupling prediction. In order to account for these, we suggest a general polynomial description of the spectral shape at "soft" photon masses. The parameters of the interpolation are determined though a least-squares fit to the lattice data at large imaginary-time separations. Subsequently the fit result can be employed in order to extract spectral information concerning the soft domain.

This paper is organized as follows. After discussing what is known theoretically about the vector channel spectral function in various regimes in sec. 2, we introduce a general polynomial interpolation, designed to describe the soft regime, in sec. 3. The lattice analysis, incorporating a continuum extrapolation at three non-zero momenta and two temperatures, is described in sec. 4. Our fitting strategy and the corresponding results are presented in sec. 5, and we conclude in sec. 6. In an appendix the analysis is repeated for lattice data at zero momentum, pointing out that systematic uncertainties are much larger in this case.

2. Theoretical constraints on the vector channel spectral function

2.1. Basic definitions

To leading order in the electromagnetic fine structure constant but to all orders in the strong coupling, the photon production rate per unit volume can be expressed as [14, 15]

$$\frac{\mathrm{d}\Gamma_\gamma(\mathbf{k})}{\mathrm{d}^3\mathbf{k}} = \frac{1}{(2\pi)^3 2k} \sum_\lambda \epsilon^{(\lambda)}_{\mu,\mathbf{k}} \epsilon^{(\lambda)*}_{\nu,\mathbf{k}} \int_\mathcal{X} e^{i\mathcal{K}\cdot\mathcal{X}} \big\langle J^\mu_{\rm em}(0) J^\nu_{\rm em}(\mathcal{X}) \big\rangle \tag{2.1}$$

$$= \frac{1}{(2\pi)^3 2k} \int_\mathcal{X} e^{i\mathcal{K}\cdot\mathcal{X}} \Big\langle \sum_{i=1}^{3} J^i_{\rm em}(0) J^i_{\rm em}(\mathcal{X}) - J^0_{\rm em}(0) J^0_{\rm em}(\mathcal{X}) \Big\rangle \;, \tag{2.2}$$

where $\mathcal{K} \equiv (k, \mathbf{k})$, $k \equiv |\mathbf{k}|$; $\mathcal{X} \equiv (t, \mathbf{x})$; $\mathcal{K}\cdot\mathcal{X} \equiv kt - \mathbf{k}\cdot\mathbf{x}$, $\epsilon^{(\lambda)}_{\mu,\mathbf{k}}$ denote polarization vectors, and $J^\mu_{\rm em}$ is the electromagnetic current. In the second step we made use of a Ward identity, guaranteeing that longitudinal polarizations do not contribute for $\mathcal{K}^2 = 0$.

The electromagnetic current can in turn be expressed as $J^\mu_{\rm em} = e \sum_{f=1}^{N_{\rm f}} Q_f V^\mu_f$, where $V^\mu_f \equiv \bar\psi_f \gamma^\mu \psi_f$ is the vector current associated with the quark flavour f, and Q_f denotes the electric charge of flavour f in units of the elementary charge e. We consider the case of three degenerate flavours, $N_{\rm f} = 3$, so that $\sum_{f=1}^{N_{\rm f}} Q_f = 0$ and $\sum_{f=1}^{N_{\rm f}} Q_f^2 = 2/3$. Then the disconnected quark contraction drops out. Relating furthermore the Wightman correlator of eq. (2.2) to a spectral function we can write

$$\frac{\mathrm{d}\Gamma_\gamma(\mathbf{k})}{\mathrm{d}^3\mathbf{k}} = \frac{e^2 \sum_{f=1}^{N_{\rm f}} Q_f^2}{(2\pi)^3 k} \, n_{\rm B}(k)\, \rho_{\rm V}(k, \mathbf{k}) \;, \tag{2.3}$$

where $n_{\rm B}$ is the Bose distribution. The vector channel spectral function has been defined as

$$\rho_{\rm V}(\omega, \mathbf{k}) \equiv \int_\mathcal{X} e^{i(\omega t - \mathbf{k}\cdot\mathbf{x})} \Big\langle \frac{1}{2}\big[V^i(t,\mathbf{x})\,,\, V^i(0)\big] - \frac{1}{2}\big[V^0(t,\mathbf{x})\,,\, V^0(0)\big] \Big\rangle_{\rm c} \;, \tag{2.4}$$

where $\langle ... \rangle_{\rm c}$ indicates that only the connected contraction is included. The same spectral function also determines the dilepton production rate as

$$\frac{\mathrm{d}\Gamma_{\ell^-\ell^+}(\omega, \mathbf{k})}{\mathrm{d}\omega\, \mathrm{d}^3\mathbf{k}} = \frac{2e^4 \sum_f Q_f^2\, \theta(M^2 - 4m_\ell^2)}{3(2\pi)^5 M^2} \left(1 + \frac{2m_\ell^2}{M^2}\right) \left(1 - \frac{4m_\ell^2}{M^2}\right)^{\frac{1}{2}} n_{\rm B}(\omega)\, \rho_{\rm V}(\omega, \mathbf{k}) \;, \tag{2.5}$$

where the invariant mass of the dilepton pair has been defined as

$$M^2 \equiv \omega^2 - k^2 \;. \tag{2.6}$$

2.2. NLO weak-coupling expansion

In vacuum ($T = 0$, where T denotes the temperature), $\rho_{\rm V}$ is a function only of the photon invariant mass defined in eq. (2.6). The presence of a thermal plasma breaks Lorentz invariance, so that $\rho_{\rm V}$ is a function of two independent kinematic variables, $\omega \pm k$. In particular, in the non-interacting limit [16],

$$\rho_{\rm V}(\omega,\mathbf{k}) \;=\; \frac{N_{\rm c} T M^2}{2\pi k}\biggl\{ \ln\biggl[\frac{\cosh(\frac{\omega+k}{4T})}{\cosh(\frac{\omega-k}{4T})}\biggr] - \frac{\omega\,\theta(k-\omega)}{2T} \biggr\} \;, \tag{2.7}$$

where $N_{\rm c}=3$. This "Born" or "thermal Drell-Yan" rate provides for a reasonable approximation at large invariant masses, $M \gg \pi T$. However for zero invariant mass the Born rate vanishes, and the leading-order (LO) result is proportional to $\alpha_{\rm s}T^2$.

The determination of the correct LO result poses a formidable challenge [10]. However there is a logarithmically enhanced term that can be worked out analytically [7,8],

$$\rho_{\rm V}(k,\mathbf{k}) \;=\; \frac{\alpha_{\rm s} N_{\rm c} C_{\rm F} T^2}{4} \ln\biggl(\frac{1}{\alpha_{\rm s}}\biggr)\Bigl[1-2n_{\rm F}(k)\Bigr] + \mathcal{O}(\alpha_{\rm s}T^2) \;, \tag{2.8}$$

where $n_{\rm F}$ is a Fermi distribution and $C_{\rm F}\equiv (N_{\rm c}^2-1)/(2N_{\rm c})$. The non-logarithmic terms are only known in numerical form [9,10]. Recently, these results have been extended to $\mathcal{O}(\alpha_{\rm s}^{3/2}T^2)$ both at vanishing [11] and non-vanishing photon masses ($|M|\lesssim gT$, where $g\equiv\sqrt{4\pi\alpha_{\rm s}}$) [17]. In the following we make use of the results of ref. [17].

If the photon mass is large, $M\gg g^{1/2}T$, then there is a "crossover" to a different type of behaviour [17,18]. For $M\sim\pi T$ the NLO corrections are suppressed by $\alpha_{\rm s}$ and numerically small [19,20]. For $M\gg\pi T$, the spectral function goes over into a vacuum result [21] which is known to relative accuracy $\mathcal{O}(\alpha_{\rm s}^4)$ [22,23] and can directly be taken over for a thermal analysis [20,24]. Such precisely determined results play an essential role in our investigation.

2.3. Hydrodynamic regime

A special kinematic corner in which it is possible to make statements about $\rho_{\rm V}$ beyond the weak-coupling expansion is given by the so-called hydrodynamic regime, parametrically $\omega,k\lesssim\alpha_{\rm s}^2T$. This is the regime in which the general theory of statistical fluctuations [25] applies. Then the properties of $\rho_{\rm V}$ can be parametrized by a diffusion coefficient, denoted by D, and by a susceptibility, denoted by $\chi_{\rm q}$. The susceptibility determines the value of the conserved charge correlator at zero momentum, $\chi_{\rm q}\equiv\int_0^\beta{\rm d}\tau\int_{\mathbf{x}}\langle V^0(\tau,\mathbf{x})V^0(0)\rangle$, whereas D can be defined through a Kubo formula as

$$D\equiv\frac{1}{3\chi_{\rm q}}\lim_{\omega\to0^+}\sum_{i=1}^{3}\frac{\rho^{ii}(\omega,\mathbf{0})}{\omega}\;. \tag{2.9}$$

The electrical conductivity is a weighted sum over these quantities,

$$\sigma = e^2\sum_{f=1}^{N_{\rm f}} Q_f^2\chi_{\rm q}D\;, \tag{2.10}$$

where the disconnected contribution has been omitted thanks to $\sum_f Q_f = 0$.

In the hydrodynamic regime, the full $\rho_{\rm V}$ can be expressed in terms of D and $\chi_{\rm q}$. As already mentioned the longitudinal components do not contribute at the on-shell point, but they have a non-trivial diffusive structure elsewhere, leading to the prediction (cf. e.g. ref. [26])

$$\frac{\rho_{\rm V}(\omega,\mathbf{k})}{\omega} = \left(\frac{\omega^2 - k^2}{\omega^2 + D^2 k^4} + 2\right)\chi_{\rm q} D \; . \tag{2.11}$$

Consequently the photon production rate from eq. (2.3) becomes

$$\frac{\mathrm{d}\Gamma_\gamma(\mathbf{k})}{\mathrm{d}^3\mathbf{k}} \overset{k \lesssim \alpha_{\rm s}^2 T}{\approx} \frac{2T\sigma}{(2\pi)^3 k} \; . \tag{2.12}$$

We also note that, for $\omega \ll Dk^2$ and $k \ll 1/D$, eq. (2.11) predicts that

$$\lim_{\omega\to 0} \frac{\rho_{\rm V}(\omega,\mathbf{k})}{\omega} = -\frac{\chi_{\rm q}}{Dk^2} \; , \tag{2.13}$$

i.e. the slope should be negative at small enough frequencies. The reason is that for very small k, ρ^{00} resembles a Dirac delta-function, which comes with a negative sign in $\rho_{\rm V}$.[1]

2.4. AdS/CFT limit

In the AdS/CFT framework $\rho_{\rm V}$ has the same infrared structure as in eq. (2.11), with the specific values $D = 1/(2\pi T)$ and $\chi_{\rm q} = N_{\rm c}^2 T^2/8$ [27, 28]. The spectral function is close to the hydrodynamic form for $k \lesssim 0.5/D$, and becomes negative at the smallest ω for $k \lesssim 1.07/D$. Below we make use of the results of ref. [28], evaluated numerically so that they make predictions beyond the hydrodynamic regime as well. Of course, there is no reason for these predictions to be applicable to thermal QCD, and in general the results need to be rescaled to be useful at all (see below); this is why we refer to the AdS/CFT limit as a "holographic model". Nevertheless, they offer useful qualitative insight into the structures that may be expected at small ω and k in an interacting system.

3. Polynomial interpolation

As alluded to in sec. 2.2, we expect the perturbatively determined $\rho_{\rm V}$ to be least precise at *small* frequencies. For instance deep in the spacelike domain ($\omega \ll k$) only the LO result is known (cf. eq. (2.7)), but we have argued in sec. 2.3 that the true behaviour is qualitatively different, at least for very small k. Close to the light cone (for $|M| \lesssim gT$), NLO corrections are known, but they are only suppressed by $\mathcal{O}(g)$ so the weak-coupling expansion might not

[1] The physical spectral function is positive at and somewhat below the light cone [17]. According to eq. (2.13), it should cross zero at some $\omega < k$ if k is small enough, $k \lesssim \alpha_{\rm s}^2 T$. Because of unknown numerical prefactors, it is unclear whether such k are reached in our simulations.

converge well. In contrast, we may assume that the regime of large frequencies, known up to $\mathcal{O}(g^2)$ for $M \gtrsim \pi T$ and up to $\mathcal{O}(g^8)$ for $M \gg \pi T$, is better under control.

It is an interesting question whether the spectral function needs to be analytic across the light cone.[2] At zero temperature this is not the case: ρ_V vanishes identically in the spacelike domain. However, in an interacting system the spectral function gets generally smoothened by a temperature. Physical arguments in favour of smoothness at the NLO level have been presented in ref. [29], and this is also the case in the concrete NLO computation [17] as well as in the non-perturbative frameworks discussed in secs. 2.3 and 2.4. In the following, we assume ρ_V to be a smooth function across the light cone, and represent it through a polynomial interpolation on both sides.

Let ω_0 lie in the time-like domain, for instance $\omega_0 \simeq \sqrt{k^2 + (\pi T)^2}$. We introduce a polynomial starting with a linear behaviour at $\omega \ll T$ and attaching to the known ρ_V continuously and with a continuous first derivative at $\omega = \omega_0$. Defining

$$\rho_\mathrm{V}(\omega_0, \mathbf{k}) \;\equiv\; \beta \;, \quad \rho'_\mathrm{V}(\omega_0, \mathbf{k}) \;\equiv\; \gamma \;, \tag{3.1}$$

where the dimension of β is T^2 and that of γ is T, a general $(5+2n_\mathrm{max})^\mathrm{th}$ order polynomial proceeding in odd powers of ω and satisfying these boundary values can be expressed as

$$\rho_\mathrm{fit} \;\equiv\; \frac{\beta\,\omega^3}{2\omega_0^3}\left(5 - \frac{3\omega^2}{\omega_0^2}\right) - \frac{\gamma\,\omega^3}{2\omega_0^2}\left(1 - \frac{\omega^2}{\omega_0^2}\right) + \sum_{n\ge 0}^{n_\mathrm{max}} \frac{\delta_n \omega^{1+2n}}{\omega_0^{1+2n}}\left(1 - \frac{\omega^2}{\omega_0^2}\right)^2 . \tag{3.2}$$

We treat β and γ as known from perturbation theory through the matching in eq. (3.1). For $n_\mathrm{max} = 0$ there is only one free parameter in the 5th order polynomial, given by the slope at origin ($\alpha \equiv \delta_0/\omega_0$), and more generally there are $n_\mathrm{max}+1$ free parameters $(\alpha, \delta_1, \ldots)$. For $\omega > \omega_0$, a perturbative result is used (its details are explained in footnote 3).

4. Lattice analysis

4.1. Observable and parameters

In continuum notation, the imaginary-time observable measured on the lattice reads

$$G_\mathrm{V}(\tau, \mathbf{k}) \;\equiv\; \int_\mathbf{x} e^{-i\mathbf{k}\cdot\mathbf{x}} \Big\langle V^i(\tau,\mathbf{x})\, V^i(0) - V^0(\tau,\mathbf{x})\, V^0(0) \Big\rangle_\mathrm{c} \;. \tag{4.1}$$

In order to minimize discretization effects, the momentum is taken to point along one of the lattice axes. In a finite-size box momenta are of the type $k = 2\pi n/(aN_s)$, where a is the lattice spacing and n is an integer; given that $aN_\tau = 1/T$, we thus consider

$$k = 2\pi n T \times \frac{N_\tau}{N_s} \;, \tag{4.2}$$

[2] This discussion concerns the infinite-volume limit.

β_0	$N_\mathrm{s}^3 \times N_\tau$	confs	$T\sqrt{t_0}$	$T/T_\mathrm{c}\vert_{t_0}$	Tr_0	$T/T_\mathrm{c}\vert_{r_0}$
7.192	$96^3 \times 32$	314	0.2796	1.12	0.816	1.09
7.544	$144^3 \times 48$	358	0.2843	1.14	0.817	1.10
7.793	$192^3 \times 64$	242	0.2862	1.15	0.813	1.09
7.192	$96^3 \times 28$	232	0.3195	1.28	0.933	1.25
7.544	$144^3 \times 42$	417	0.3249	1.31	0.934	1.25
7.793	$192^3 \times 56$	273	0.3271	1.31	0.929	1.25

Table 1: The lattices included in the current analysis, with β_0 denoting the coefficient of the Wilson plaquette term. Simulations are carried out within quenched SU(3) gauge theory. Conversions to units of t_0 [30], r_0 [31] and T_c are based on ref. [32]. In a separate set of simulations at a somewhat higher temperature [36], spatial volume dependence has been verified to be within statistical errors.

where N_τ and N_s are the temporal and spatial lattice extents, respectively.

The set of lattice simulations considered in the present study is listed in table 1. The aspect ratio was kept fixed at $N_s/N_\tau = 3$ for $T = 1.1T_\mathrm{c}$ and at $N_s/N_\tau = 24/7$ for $T = 1.3T_\mathrm{c}$. Employing $n \in \{1,2,3\}$ in eq. (4.2) the momenta were thus $k/T \in \{2.094, 4.189, 6.283\}$ and $k/T \in \{1.833, 3.665, 5.498\}$ for $T = 1.1T_\mathrm{c}$ and $T = 1.3T_\mathrm{c}$, respectively. In order to consider smaller momenta, relevant for reaching the hydrodynamic regime, larger N_s should be simulated. On the other hand, for the phenomenology of photon production, these values appear to be quite reasonable.

Our measurements were separated by 500 sweeps, each consisting of 1 heatbath and 4 overrelaxation updates. However, the large values $\beta_0 \gtrsim 7.2$ needed imply that topological degrees of freedom do not thermalize properly even with this much updating, so that in general errors may be underestimated [33]. Given that at $T > T_\mathrm{c}$ the physical value of the topological susceptibility is small and that our observables should not couple much to the slow modes, we do not expect to be significantly affected by this problem, even if in practice our simulations are frozen to the trivial topological sector.

4.2. Continuum extrapolation

For the lattice analysis we employed a local discretization of the vector current, with non-perturbatively clover-improved Wilson fermions [34, 35]. As discussed in sec. 2.1, only the connected quark contraction needs to be evaluated for the observable that we are interested in. The general techniques of the lattice analysis have been discussed in ref. [36], and the ensemble employed for our numerical investigation in ref. [37].

We carry out a continuum extrapolation for the ratios $G_\mathrm{V}(\tau,\mathbf{k})T^2/[\chi_\mathrm{q} G_\mathrm{V,free}(\tau,\mathbf{0})]$, where

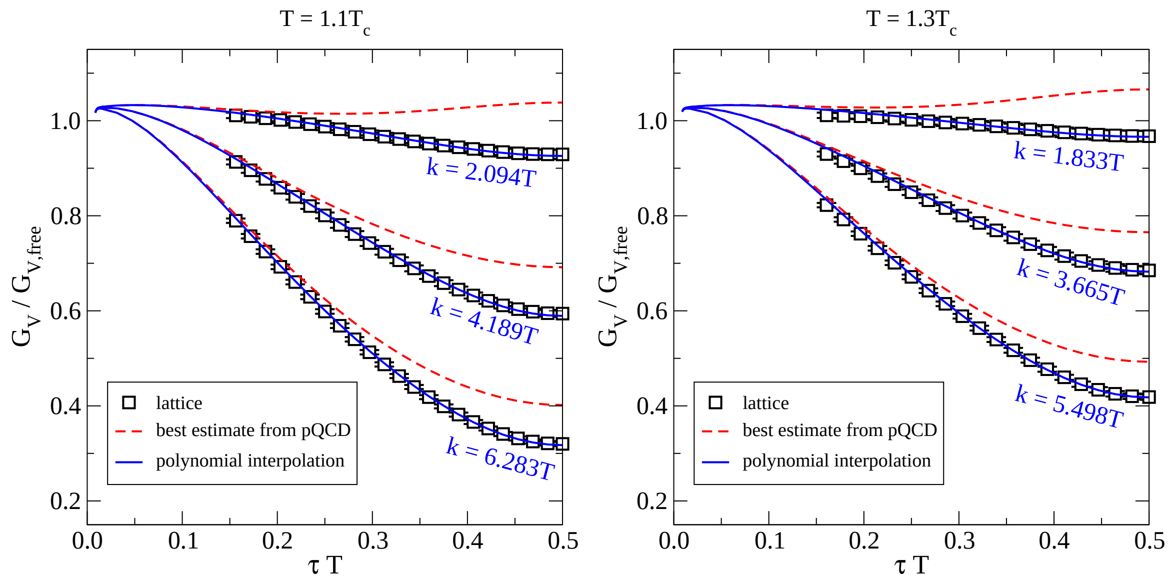

Figure 1: Fitted imaginary-time correlators at non-zero momenta. The "best estimate from pQCD" (perturbative QCD) is based on refs. [17, 18, 20], and has been constructed as explained in footnote 3. "Polynomial interpolations" correspond to $n_{\max} = 0$, but similarly good fits are obtained for $n_{\max} = 1$.

$\chi_{\rm q}$ is the quark number susceptibility and

$$G_{\rm V,free}(\tau,\mathbf{0}) \;\equiv\; 6T^3\left[\pi(1-2\tau T)\frac{1+\cos^2(2\pi\tau T)}{\sin^3(2\pi\tau T)}+\frac{2\cos(2\pi\tau T)}{\sin^2(2\pi\tau T)}\right]. \tag{4.3}$$

Normalization by $\chi_{\rm q}$ removes the renormalization factors associated with our local discretization of the vector current, and normalization through $G_{\rm V,free}$ hides the short-distance growth of the imaginary-time correlator. $\mathcal{O}(a)$ improvement permits for a continuum extrapolation quadratic in $1/N_\tau$. More details can be found in ref. [37]. With this approach a continuum extrapolation could be carried out at $\tau T \geq 0.18$ for $T = 1.1T_c$ and at $\tau T \geq 0.22$ for $T = 1.3T_c$. These are the distances included in the subsequent analysis. A bootstrap sample was generated for the continuum extrapolated results, which was used for estimating the statistical errors of our final observables. In a separate set of continuum extrapolations, the susceptibilities were determined through a quadratic fit, yielding $\chi_{\rm q} = 0.857(16)T^2$ at $T = 1.1T_{\rm c}$ and $\chi_{\rm q} = 0.897(17)T^2$ at $T = 1.3T_{\rm c}$ [37].

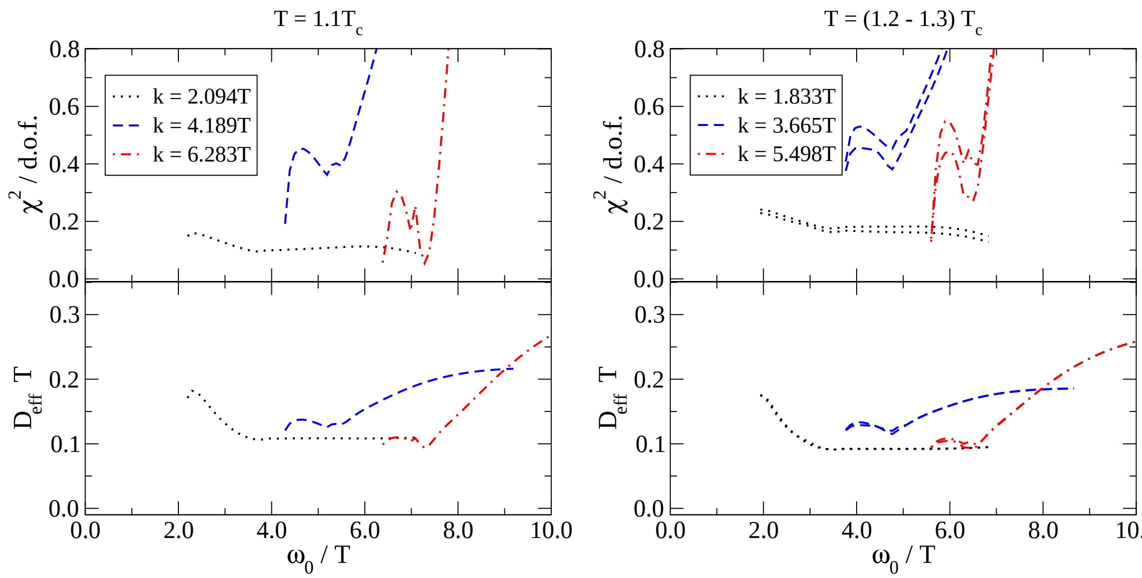

Figure 2: We show χ^2/d.o.f. (top) and $D_{\rm eff}T$ (bottom; cf. eq. (5.2)) as a function of the matching point ω_0 for $n_{\rm max} = 0$. In the right panel, the upper curves are for $T = 1.2T_{\rm c}$ and the lower curves for $T = 1.3T_{\rm c}$ on the perturbative side (the lattice data is fixed but it is not known precisely to which temperature it corresponds, cf. table 1). A local minimum of χ^2/d.o.f. is generally found close to the point where $\omega_0 = \sqrt{k^2 + (\pi T)^2}$; it is very shallow for the smallest k.

5. Fit results

Having discussed the spectral function on one side (sec. 3) and the imaginary-time correlator on the other (sec. 4), the remaining task is to compare the two. The relation is given by

$$G_{\rm V}(\tau,\mathbf{k}) = \int_0^\infty \frac{{\rm d}\omega}{\pi}\, \rho_{\rm V}(\omega,\mathbf{k})\, \frac{\cosh[\omega(\frac{\beta}{2}-\tau)]}{\sinh[\frac{\omega\beta}{2}]}\;, \quad \beta \equiv \frac{1}{T}\;. \tag{5.1}$$

Inserting into eq. (5.1) the best available perturbative estimate for $\rho_{\rm V}$, based on an interpolation between the results of refs. [17, 18, 20],[3] a visible discrepancy is observed between the perturbative and lattice results at $\tau T \gtrsim 0.3$ (cf. fig. 1). In general the lattice results are *below*

[3]The data is available through ref. [38]. More precisely, for very large time-like frequencies it is given by the large-M results of ref. [20] which go over into the N^{4}LO vacuum result for $\omega \gg \pi T$ [21–23]. For $\omega \lesssim 10T$ it is given by the interpolation of the large-M result and the LO LPM-resummed small-M result, as presented in ref. [18], summed together with the NLO small-M result of ref. [17] (switched off exponentially with growing M to avoid OPE-violating contributions [21] proportional to T^2). In this way, the value at the real photon point $\omega = k$ agrees with the NLO photon calculation [11]. In the space-like region the spectral function is the largest between the Born one with vacuum corrections [20] and the NLO small-M result [17]. In practice, this implies that at the smallest ω we have the Born-like spectral function, whereas close to the light-cone we have the small-M one, ensuring continuity across the light-cone.

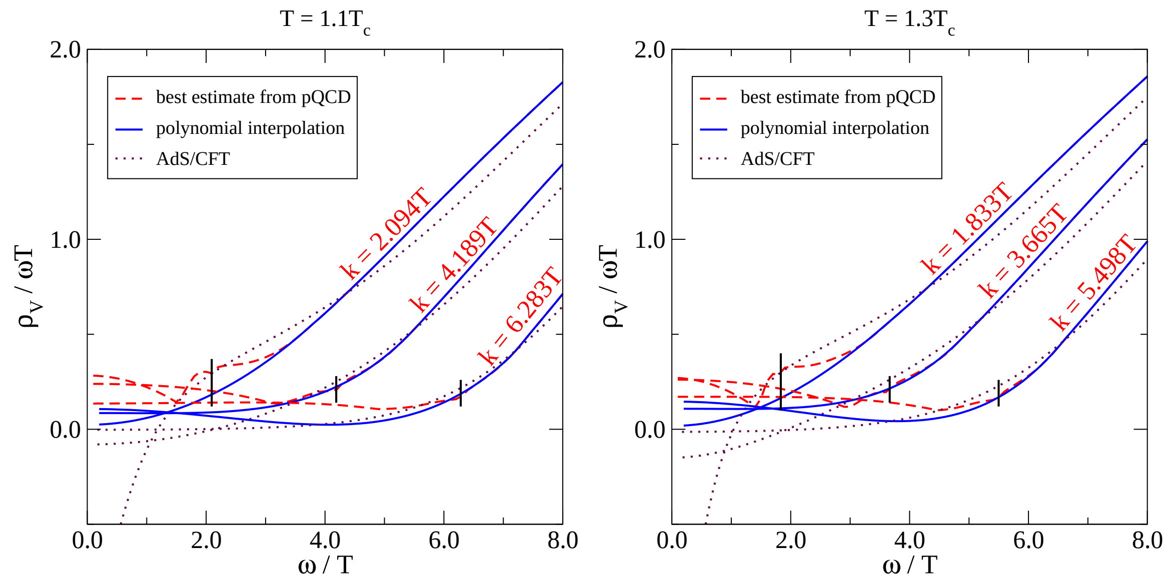

Figure 3: The spectral functions corresponding to fig. 1 ($n_{\rm max} = 0$). The vertical bars locate the light cone. The "best estimate from pQCD" is based on refs. [17, 18, 20], and has been constructed as explained in footnote 3. The AdS/CFT result comes from ref. [28], and has been rescaled to agree with the non-interacting QCD result at large ω/T. (This rescaling choice is rather arbitrary.)

the perturbative ones. The goal now is to test whether the discrepancy could be explained by modifications of $\rho_{\rm V}$ in the domain of small frequencies, as explained in sec. 3.

With the ansatz of eq. (3.2), a good representation of the data can indeed be obtained. This is illustrated in fig. 1 and more quantitatively in fig. 2, which shows the dependence of χ^2 on the matching point ω_0. In the following, we fix $\omega_0 = \sqrt{k^2 + (\pi T)^2}$, which is close to the local minimum of χ^2. Similarly small χ^2 could be obtained with $\omega_0 = k$, where the curves start, but we prefer to use the minimum that is deeper in the perturbative domain, because then we have more reasons to trust the perturbative prediction.

The corresponding results for the spectral function are illustrated in fig. 3. Barring the possibility of large non-perturbative effects at $M \gtrsim \pi T$, it appears plausible from fig. 3 that the pQCD spectral functions have too much weight in the spacelike domain. This is in qualitative agreement with the discussion in secs. 2.3 and 2.4, and suggests the gradual onset of hydrodynamics-like behaviour. That the fit lies below the perturbative curves at $k \lesssim 3T$ is also consistent with the expectation that the diffusion coefficient D of a strongly coupled system should be smaller than the result of a leading-order weak-coupling analysis [39].

The value of the spectral function at the photon point, normalized as $\rho_{\rm V}(k, \mathbf{k})T/(2\chi_{\rm q} k)$, is shown in fig. 2 (lower panels) and in fig. 4. More precisely, in order to accommodate data

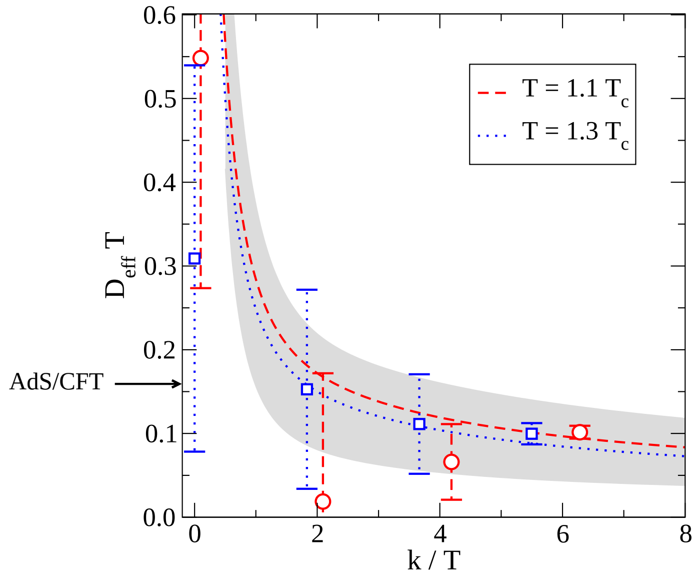

Figure 4: Lattice results for $D_{\rm eff}$ defined in eq. (5.2) (data points), compared with the NLO perturbative prediction from ref. [17] (continuous curves). The lattice errors have been obtained by carrying out fits with $n_{\rm max} = 1$ to the bootstrap ensemble. The data points at $k = 0$ (cf. appendix A) have been slightly displaced for better visibility. For comparison note that the heavy-quark diffusion coefficient, determined with different methods, has been estimated as $DT \sim 0.6...1.1$ at $T \sim 1.5T_{\rm c}$ [40], and the light-quark value as $DT \sim 0.2...0.8$ at $T = 1.1T_{\rm c}$ and $DT \sim 0.2...0.5$ at $T = 1.3T_{\rm c}$ [37]. The predictions of ref. [17] are only reliable for $k \gg gT$, but LO perturbative values at $k = 0$ can be obtained by dividing the results of ref. [39] through the lattice susceptibility according to eq. (2.9), yielding $DT \approx 2.9$ at $T = 1.1T_{\rm c}$ and $DT \approx 3.1$ at $T = 1.3T_{\rm c}$. The AdS/CFT value is $DT = 1/(2\pi)$ [27].

both at $k = 0$ and at $k > 0$, we define

$$D_{\rm eff}(k) \;\equiv\; \left\{ \begin{array}{ll} \dfrac{\rho_{\rm V}(k,\mathbf{k})}{2\chi_{\rm q} k} & , \quad k > 0 \\[2ex] \lim\limits_{\omega\to 0^+} \dfrac{\rho^{ii}(\omega,\mathbf{0})}{3\chi_{\rm q}\omega} & , \quad k = 0 \end{array} \right. . \tag{5.2}$$

According to eqs. (2.9) and (2.11), $\lim_{k\to 0} D_{\rm eff}(k) = D$. Even though the evidence for a continuous behaviour is not overwhelming in fig. 4 due to the large systematic uncertainties at small $k \lesssim 3T$, it is not excluded either. We recall that according to the discussion in sec. 2.4, hydrodynamic behaviour is expected to set in for $k \lesssim 1/D$, which according to the $k = 0$ results in fig. 4 roughly speaking corresponds to $k \lesssim 2T$.

As already alluded to, our analysis contains systematic as well as statistical uncertainties. In order get an impression about their magnitudes, the following tests have been carried out:

- We have tested the dependence of the results on the order of the fitted polynomial, parametrized by $n_{\rm max}$ in eq. (3.2). Obviously, given the ill-posed nature of the inversion

T/T_c	k/T	α/T	β/T^2	γ/T	$TD_{\rm eff}\vert_{n_{\max}=0}$	$TD_{\rm eff}\vert_{n_{\max}=1}$
1.1	2.094	0.028(15)	2.072	1.611	0.108(4)	0.019(153)
	4.189	0.091(8)	2.325	1.963	0.130(1)	0.066(45)
	6.283	0.105(4)	2.498	2.331	0.109(1)	0.102(8)
1.3	1.833	0.024(17)	2.038	1.558	0.093(5)	0.153(119)
	3.665	0.112(10)	2.229	1.984	0.119(1)	0.111(59)
	5.498	0.141(6)	2.367	2.438	0.094(1)	0.097(13)

Table 2: Fit results for the coefficients in eq. (3.2), with $\alpha = \delta_0/\omega_0$, and for the effective diffusion coefficient $D_{\rm eff}$ of eq. (5.2), from fits with $n_{\max} = 0$. For $D_{\rm eff}$ the results from the bootstrap analysis with $n_{\max} = 1$ are also shown; the latter constitute our final results and are illustrated in fig. 4.

problem, the results are quite sensitive to $n_{\max}$. The difference of the results obtained with $n_{\max} = 0$ and $n_{\max} = 1$ can be employed as one indication of systematic errors, cf. table 2. The resulting errors are of the same order of magnitude but somewhat smaller than those obtained from the bootstrap sample with $n_{\max} = 1$, cf. table 2 and the discussion below. Therefore we display the latter as our uncertainties in fig. 4. Stable results (i.e. results with errors below 100%) could only be obtained for $k \gtrsim 3T$.

- On the lattice side, uncertainties related to scale fixing imply a certain uncertainty of the value of T/T_c simulated, cf. table 1. On the perturbative side, there is an uncertainty from higher orders in the perturbative expansion, which can partly be estimated through the dependence of the results on the renormalization scale. Our experience suggests that the latter scale uncertainty (which is a higher-order effect) is of a similar magnitude as the former (which is a leading-order effect but with a smaller variation). We show results from a variation of the former type in the right panel of fig. 2, concluding that this uncertainty is negligible compared with the dependence on $n_{\max}$.

- As mentioned above, our continuum extrapolations were carried out for the ratios $T^2 G_V/[\chi_q\, G_{V,\rm free}]$, and the continuum value of χ_q/T^2 was determined through a separate extrapolation. For a matching to perturbative results in the ultraviolet regime, we need the value of G_V/T^3. In other words, the errors related to the two separate continuum extrapolations need to be combined. We have done this by fixing χ_q/T^2 to its central, minimal, and maximal value within the error band, and repeating the bootstrap analysis in each case. The resulting variations of $D_{\rm eff}T$ are subleading compared with systematic uncertainties, and can be omitted in practice.

- In figs. 1 and 5, the errors shown for the lattice data correspond to diagonal entries of the covariance matrix. However, we have carried out a full-fledged bootstrap analysis.

Bootstrap samples were used for constructing a covariance matrix in the τ-regime where the continuum extrapolation was judged to be reliable. The inverse of the covariance matrix was employed in order to determine the χ^2-value of a fit of any individual configuration to our ansatz. The resulting distribution was used for obtaining errors for D_{eff}, shown in fig. 4. The results obtained with $n_{\max} = 0$ and $n_{\max} = 1$ are given in table 2. The errors of the $n_{\max} = 1$ results encompass in general the central values of the $n_{\max} = 0$ results, and constitute our best estimate of uncertainties.

6. Conclusions

We have shown how a combination of lattice and perturbative results allows us to obtain non-trivial information about the vector channel spectral function close to the photon point. The results are conveniently displayed in terms of the function $D_{\text{eff}}(k)$, defined in eq. (5.2). The observed small difference between the fit and the perturbative result at $k \gtrsim 3T$, cf. fig. 4, is consistent with the smallness of the NLO correction [11, 17], as well as with indirect cross-checks concerning the convergence of the weak-coupling expansion for light-cone observables at $k \gtrsim 2\pi T$, based on measuring screening masses at non-zero Matsubara frequencies [41].

We have demonstrated that, even though not constrained to do so *a priori*, the fit result reproduces some qualitative features expected from the soft domain, namely a reduced (and possibly even negative) spectral weight in the spacelike domain, cf. fig. 3. Basically, the best fit result lies between the pQCD and the strong-coupling AdS/CFT predictions.

As has been illustrated in fig. 4, measurements at non-zero momenta may offer for an alternative way to estimate the diffusion coefficient, avoiding possible problems of the standard approach [36,37,42–46] which have to deal with a very narrow transport peak at zero momentum [47]. However, for a quantitative study, much smaller values of k should be reached with controlled errors. It would be interesting to test whether the analytic improvement program of ref. [48] could help in this. Conceivably, a similar methodology could also be employed for estimating other transport coefficients, such as the shear viscosity of the QCD plasma.

Our analysis made use of continuum-extrapolated lattice data for quenched QCD ($N_{\rm f} = 0$). However, the qualitative lessons are expected to remain valid also for unquenched QCD.

In terms of the quantity $D_{\text{eff}}(k)$ defined in eq. (5.2) and shown in fig. 4, the physical photon rate from eq. (2.3) can be expressed as (for $N_{\rm f} = 3$)

$$\frac{{\rm d}\Gamma_\gamma(\mathbf{k})}{{\rm d}^3\mathbf{k}} = \frac{2\alpha_{\rm em}\chi_{\rm q}}{3\pi^2}\, n_{\rm B}(k) D_{\text{eff}}(k) \; . \tag{6.1}$$

Here $\chi_{\rm q} \lesssim T^2$ is a light quark number susceptibility, and $n_{\rm B}$ is the Bose distribution. The parametrization in eq. (6.1) should be useful for phenomenological analyses as well. In particular, given that D_{eff} is a decreasing function of k, the soft photon production rate increases at small k even faster than the naive estimate ${\rm d}\Gamma_\gamma/{\rm d}^3\mathbf{k} \sim \alpha_{\rm em} T n_{\rm B}(k)$.

To summarize, the present results support the program of implementing pQCD results into hydrodynamical codes [49–51]. The theoretical uncertainties could be as low as $\sim 20\%$, save for soft $k \lesssim 2T$ where the pQCD results represent an overestimate (cf. fig. 4). It is remarkable that such an overshooting is in apparent qualitative agreement with phenomenology [50]. In light of the photon v_2 puzzle, it would be interesting to extend the investigation down to lower temperatures, even though this is well justified only in the presence of dynamical quarks and even though at low temperatures the spectral function ansatz should include the possibility of vector resonance contributions.

Acknowledgments

We thank G.D. Moore for providing us his codes related to refs. [28, 47] and for helpful comments on the manuscript. The work has been supported by the DFG under grant GRK881, by the SNF under grant 200020-155935, by the European Union through HadronPhysics3 (grant 283286) and ITN STRONGnet (grant 238353), and by the Väisälä Foundation. Simulations were performed using JARA-HPC resources at the RWTH Aachen and JSC Jülich (projects JARA0039 and JARA0108), the OCuLUS Cluster at the Paderborn Center for Parallel Computing, and the Bielefeld GPU cluster.

Appendix A. Results for zero momentum

The extraction of transport coefficients at vanishing momentum, $k = 0$, is faced with several challenges. One is that the transport peak could be very narrow [47] and therefore difficult to resolve from an imaginary-time measurement. A separate problem is related to the domain of large frequencies, whose insufficient treatment may "contaminate" the extraction of spectral features at low frequencies [24]. The latter problem can be alleviated by making use of similar methods as discussed in the main body of our paper. Numerical "best estimate from pQCD" spectral functions that can be used for this purpose, based on refs. [24, 47, 52], have been tabulated in ref. [38].[4] In this appendix we show the results that we obtain if the small-frequency domain is subsequently modelled through eq. (3.2).

[4]More precisely, these results have been obtained by combining the Born result with N^4LO vacuum corrections [22, 23], valid for $\omega \gg \pi T$ [21], with the NLO result valid for $\omega \sim \pi T$ [52], and then taking the largest between this combination and the $\omega \sim \alpha_s^2 T$ result [47], featuring a perturbative transport peak. In this way at small ω we obtain a transport peak, at intermediate ω the LO+NLO sum, and at large ω the N^4LO asymptotics. We have checked that the results of ref. [52] agree with the $k \to 0$ limit of the NLO correction in ref. [20], once the partial resummation of the thermal mass performed in ref. [52] is undone, being unjustified for $\omega \gtrsim \pi T$. For what concerns the transport peak, we have "quenched" the calculation of ref. [47] by removing $2 \leftrightarrow 2$ processes with more than 2 external fermion lines from the collision operator and by fixing the Debye mass to its $N_\mathrm{f} = 0$ value.

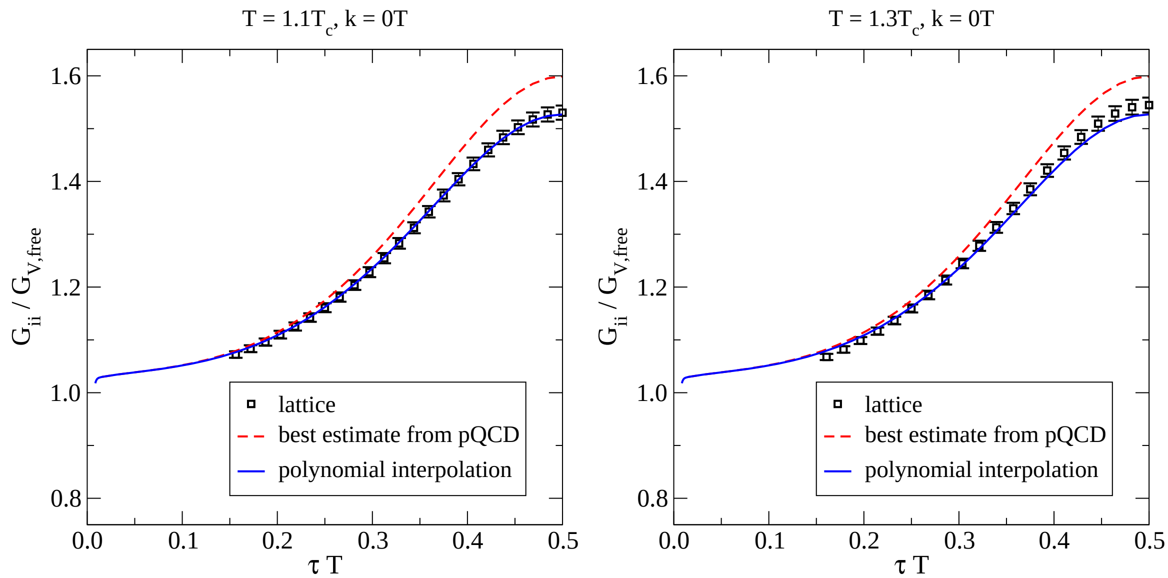

Figure 5: Like in fig. 1 but at zero momentum. Only the spatial components of the vector current have been included here. The "best estimate from pQCD" is based on refs. [24, 47, 52], and has been constructed as explained in footnote 4.

Like at non-zero momentum, the procedure described leads to a reasonably good description of the imaginary-time correlators at $\tau T \gtrsim 0.2$ (χ^2/d.o.f. $\gtrsim 1.4$). This is illustrated in fig. 5, with the corresponding spectral functions shown in fig. 6. The diffusion coefficient, defined through eq. (2.9), is displayed in fig. 4, as obtained from the bootstrap sample with $n_{\rm max} = 1$.

It must be stressed, however, that our results at $k = 0$ suffer from substantial systematic uncertainties. Indeed, if we fix $n_{\rm max} = 0$ and vary the fitting point, like in fig. 2, then χ^2/d.o.f. does not show a minimum but rather increases as a function of ω_0. It is rather flat for $\omega_0 \lesssim T$, however then the transport peak is narrower than shown in fig. 6 and correspondingly the value of the intercept at $\omega = 0$ is larger (the area under the transport peak remains roughly constant). More quantitatively, values up to $\rho_{ii}/(\omega T) \lesssim 4.5$ can be obtained with χ^2/d.o.f. ~ 1.4 for $\omega_0 \lesssim T$; this corresponds to $DT \lesssim 1.8$. We conclude that the narrowness of the transport peak at $k = 0$ poses a formidable challenge which is not solved by our approach. Finally we remark that in a companion paper [37] different ansätze led to the estimates $\rho_{ii}/(\omega T) \sim 0.6...2.1$ at $T = 1.1T_{\rm c}$ and $\rho_{ii}/(\omega T) \sim 0.6...1.2$ at $T = 1.3T_{\rm c}$, which are quite consistent with fig. 6 (note that the normalization of ρ_{ii} in ref. [37] differs by a factor 2 from the present paper).

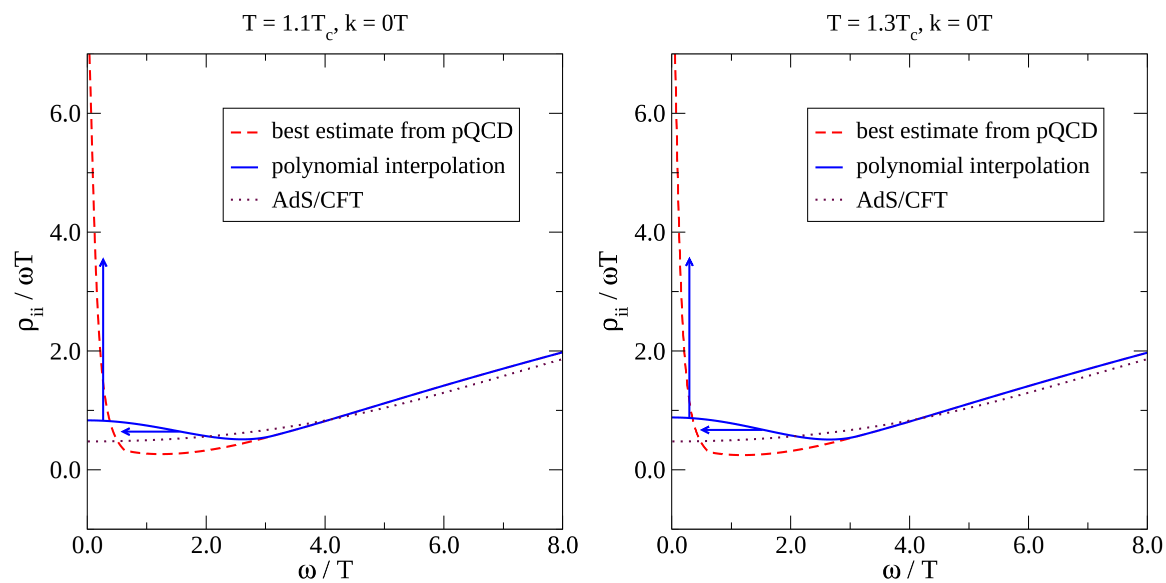

Figure 6: The spectral functions corresponding to fig. 5 from fits with $n_{\max} = 0$. The "best estimate from pQCD" is based on refs. [24, 47, 52], and has been constructed as explained in footnote 4. The AdS/CFT result comes from ref. [28], and has been rescaled to agree with the non-interacting QCD result at large ω/T (cf. caption of fig. 3). As discussed in appendix A and illustrated with the arrows, the intercepts at $\omega = 0$ are lower bounds, and the widths of the transport peaks are upper bounds.

References

[1] A. Adare *et al.* [PHENIX Collaboration], *Centrality dependence of low-momentum direct-photon production in Au+Au collisions at* $\sqrt{s_{NN}} = 200\ GeV$, Phys. Rev. C 91 (2015) 064904 [1405.3940].

[2] A. Adare *et al.* [PHENIX Collaboration], *Dielectron production in Au+Au collisions at* $\sqrt{s_{NN}}$*=200 GeV,* Phys. Rev. C 93 (2016) 014904 [1509.04667].

[3] J. Adam *et al.* [ALICE Collaboration], *Direct photon production in Pb-Pb collisions at* $\sqrt{s_{\rm NN}} = 2.76$ *TeV,* Phys. Lett. B 754 (2016) 235 [1509.07324].

[4] L.D. McLerran and T. Toimela, *Photon and Dilepton Emission from the Quark-Gluon Plasma: Some General Considerations,* Phys. Rev. D 31 (1985) 545.

[5] H.A. Weldon, *Reformulation of Finite Temperature Dilepton Production,* Phys. Rev. D 42 (1990) 2384.

[6] C. Gale and J.I. Kapusta, *Vector dominance model at finite temperature,* Nucl. Phys. B 357 (1991) 65.

[7] J.I. Kapusta, P. Lichard and D. Seibert, *High-energy photons from quark-gluon plasma versus hot hadronic gas,* Phys. Rev. D 44 (1991) 2774; *ibid.* 47 (1993) 4171 (E).

[8] R. Baier, H. Nakkagawa, A. Niégawa and K. Redlich, *Production rate of hard thermal photons and screening of quark mass singularity,* Z. Phys. C 53 (1992) 433.

[9] P.B. Arnold, G.D. Moore and L.G. Yaffe, *Photon emission from ultrarelativistic plasmas,* JHEP 11 (2001) 057 [hep-ph/0109064].

[10] P.B. Arnold, G.D. Moore and L.G. Yaffe, *Photon emission from quark gluon plasma: Complete leading order results,* JHEP 12 (2001) 009 [hep-ph/0111107].

[11] J. Ghiglieri *et al*, *Next-to-leading order thermal photon production in a weakly coupled quark-gluon plasma,* JHEP 05 (2013) 010 [1302.5970].

[12] I. Ghisoiu, J. Möller and Y. Schröder, *Debye screening mass of hot Yang-Mills theory to three-loop order,* JHEP 11 (2015) 121 [1509.08727].

[13] G. Cuniberti, E. De Micheli and G.A. Viano, *Reconstructing the thermal Green functions at real times from those at imaginary times,* Commun. Math. Phys. 216 (2001) 59 [cond-mat/0109175].

[14] M. Le Bellac, *Thermal Field Theory* (Cambridge University Press, Cambridge, 2000).

[15] J.I. Kapusta and C. Gale, *Finite-Temperature Field Theory: Principles and Applications* (Cambridge University Press, Cambridge, 2006).

[16] G. Aarts and J.M. Martínez Resco, *Continuum and lattice meson spectral functions at nonzero momentum and high temperature,* Nucl. Phys. B 726 (2005) 93 [hep-lat/0507004].

[17] J. Ghiglieri and G.D. Moore, *Low Mass Thermal Dilepton Production at NLO in a Weakly Coupled Quark-Gluon Plasma,* JHEP 12 (2014) 029 [1410.4203].

[18] I. Ghisoiu and M. Laine, *Interpolation of hard and soft dilepton rates,* JHEP 10 (2014) 83 [1407.7955].

[19] M. Laine, *Thermal 2-loop master spectral function at finite momentum,* JHEP 05 (2013) 083 [1304.0202].

[20] M. Laine, *NLO thermal dilepton rate at non-zero momentum,* JHEP 11 (2013) 120 [1310.0164].

[21] S. Caron-Huot, *Asymptotics of thermal spectral functions,* Phys. Rev. D 79 (2009) 125009 [0903.3958].

[22] P.A. Baikov, K.G. Chetyrkin and J.H. Kühn, *Order α_s^4 QCD Corrections to Z and τ Decays,* Phys. Rev. Lett. 101 (2008) 012002 [0801.1821].

[23] P.A. Baikov, K.G. Chetyrkin, J.H. Kühn and J. Rittinger, *Adler Function, Sum Rules and Crewther Relation of Order $O(\alpha_s^4)$: the Singlet Case,* Phys. Lett. B 714 (2012) 62 [1206.1288].

[24] Y. Burnier and M. Laine, *Towards flavour diffusion coefficient and electrical conductivity without ultraviolet contamination,* Eur. Phys. J. C 72 (2012) 1902 [1201.1994].

[25] E.M. Lifshitz and L.P. Pitaevskii, *Statistical Physics, Part 2*, §88-89 (Butterworth-Heinemann, Oxford).

[26] J. Hong and D. Teaney, *Spectral densities for hot QCD plasmas in a leading log approximation,* Phys. Rev. C 82 (2010) 044908 [1003.0699].

[27] G. Policastro, D.T. Son and A.O. Starinets, *From AdS / CFT correspondence to hydrodynamics,* JHEP 09 (2002) 043 [hep-th/0205052].

[28] S. Caron-Huot *et al*, *Photon and dilepton production in supersymmetric Yang-Mills plasma,* JHEP 12 (2006) 015 [hep-th/0607237].

[29] S. Caron-Huot, *$O(g)$ plasma effects in jet quenching,* Phys. Rev. D 79 (2009) 065039 [0811.1603].

[30] M. Lüscher, *Properties and uses of the Wilson flow in lattice QCD,* JHEP 08 (2010) 071; *ibid.* 03 (2014) 092 (E) [1006.4518].

[31] R. Sommer, *A New way to set the energy scale in lattice gauge theories and its applications to the static force and $\alpha_{\rm s}$ in SU(2) Yang-Mills theory,* Nucl. Phys. B 411 (1994) 839 [hep-lat/9310022].

[32] A. Francis *et al*, *Critical point and scale setting in SU(3) plasma: An update,* Phys. Rev. D 91 (2015) 096002 [1503.05652].

[33] S. Schaefer *et al.* [ALPHA Collaboration], *Critical slowing down and error analysis in lattice QCD simulations,* Nucl. Phys. B 845 (2011) 93 [1009.5228].

[34] M. Lüscher *et al*, *Non-perturbative $O(a)$ improvement of lattice QCD,* Nucl. Phys. B 491 (1997) 323 [hep-lat/9609035].

[35] M. Lüscher, S. Sint, R. Sommer and H. Wittig, *Non-perturbative determination of the axial current normalization constant in $O(a)$ improved lattice QCD,* Nucl. Phys. B 491 (1997) 344 [hep-lat/9611015].

[36] H.-T. Ding *et al*, *Thermal dilepton rate and electrical conductivity: An analysis of vector current correlation functions in quenched lattice QCD,* Phys. Rev. D 83 (2011) 034504 [1012.4963].

[37] H.T. Ding, O. Kaczmarek and F. Meyer, *Thermal dilepton rates and electrical conductivity of QGP from the lattice,* 1604.06712.

[38] J. Ghiglieri and M. Laine, web page *Data for the thermal vector channel spectral function,* `http://www.laine.itp.unibe.ch/dilepton-lattice/`.

[39] P.B. Arnold, G.D. Moore and L.G. Yaffe, *Transport coefficients in high temperature gauge theories. (II) Beyond leading log,* JHEP 05 (2003) 051 [hep-ph/0302165].

[40] A. Francis *et al*, *A non-perturbative estimate of the heavy quark momentum diffusion coefficient,* Phys. Rev. D 92 (2015) 116003 [1508.04543].

[41] B.B. Brandt, A. Francis, M. Laine and H.B. Meyer, *A relation between screening masses and real-time rates,* JHEP 05 (2014) 117 [1404.2404].

[42] S. Gupta, *The Electrical conductivity and soft photon emissivity of the QCD plasma,* Phys. Lett. B 597 (2004) 57 [hep-lat/0301006].

[43] G. Aarts *et al*, *Spectral functions at small energies and the electrical conductivity in hot, quenched lattice QCD,* Phys. Rev. Lett. 99 (2007) 022002 [hep-lat/0703008].

[44] B.B. Brandt, A. Francis, H.B. Meyer and H. Wittig, *Thermal Correlators in the ρ channel of two-flavor QCD,* JHEP 03 (2013) 100 [1212.4200].

[45] G. Aarts *et al*, *Electrical conductivity and charge diffusion in thermal QCD from the lattice,* JHEP 02 (2015) 186 [1412.6411].

[46] B.B. Brandt, A. Francis, B. Jaeger and H.B. Meyer, *Charge transport and vector meson dissociation across the thermal phase transition in lattice QCD with two light quark flavors,* Phys. Rev. D 93 (2016) 054510 [1512.07249].

[47] G.D. Moore and J.-M. Robert, *Dileptons, spectral weights, and conductivity in the quark-gluon plasma,* hep-ph/0607172.

[48] F. Ferrari, *The Analytic Renormalization Group,* 1602.07355.

[49] G. Vujanovic *et al*, *Dilepton emission in high-energy heavy-ion collisions with viscous hydrodynamics,* Phys. Rev. C 89 (2014) 034904 [1312.0676].

[50] Y. Burnier and C. Gastaldi, *The contribution of NLO and LPM corrections to thermal dilepton emission in heavy ion collisions,* Phys. Rev. C 93 (2016) 044902 [1508.06978].

[51] J.F. Paquet *et al*, *The production of photons in relativistic heavy-ion collisions,* Phys. Rev. C 93 (2016) 044906 [1509.06738].

[52] T. Altherr and P. Aurenche, *Finite temperature QCD corrections to lepton-pair formation in a quark-gluon plasma,* Z. Phys. C 45 (1989) 99.